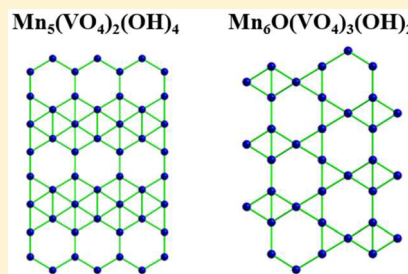


Honeycomb-like  $S = 5/2$  Spin–Lattices in Manganese(II) VanadatesLiurukara. D. Sanjeewa,<sup>†</sup> Michael A. McGuire,<sup>‡</sup> Colin D. McMillen,<sup>†</sup> Daniel Willett,<sup>†</sup> George Chumanov,<sup>†</sup> and Joseph W. Kolis<sup>\*,†</sup><sup>†</sup>Department of Chemistry and Center for Optical Materials Science and Engineering Technologies, Clemson University, Clemson, South Carolina 29634-0973, United States<sup>‡</sup>Materials Science and Technology Division, Oak Ridge National Laboratory, Oak Ridge, Tennessee 37831, United States

## Supporting Information

**ABSTRACT:** New complex manganese vanadate materials were synthesized as high-quality single crystals in multi-millimeter lengths using a high-temperature, high-pressure hydrothermal method. One compound,  $\text{Mn}_5(\text{VO}_4)_2(\text{OH})_4$ , was grown from  $\text{Mn}_2\text{O}_3$  and  $\text{V}_2\text{O}_5$  in 3 M CsOH at 580 °C and 1.5 kbar. Changing the mineralizer to 1 M CsOH/3M CsCl leads to the formation of another product,  $\text{Mn}_6\text{O}(\text{VO}_4)_2(\text{OH})$ . Both compounds were structurally characterized by single-crystal X-ray diffraction ( $\text{Mn}_5(\text{VO}_4)_2(\text{OH})_4$ :  $C2/m$ ,  $Z = 2$ ,  $a = 9.6568(9)$  Å,  $b = 9.5627(9)$  Å,  $c = 5.4139(6)$  Å,  $\beta = 98.529(8)^\circ$ ;  $\text{Mn}_6\text{O}(\text{VO}_4)_2(\text{OH})$ :  $P2_1/m$ ,  $Z = 2$ ,  $a = 8.9363(12)$  Å,  $b = 6.4678(8)$  Å,  $c = 10.4478(13)$  Å,  $\beta = 99.798(3)^\circ$ ), revealing interesting low-dimensional transition-metal features.  $\text{Mn}_5(\text{VO}_4)_2(\text{OH})_4$  possesses complex honeycomb-type Mn–O layers, built from edge-sharing  $[\text{MnO}_6]$  octahedra in the  $bc$  plane, with bridging vanadate groups connecting these layers along the  $a$ -axis.  $\text{Mn}_6\text{O}(\text{VO}_4)_2(\text{OH})$  presents a more complicated structure with both octahedral  $[\text{MnO}_6]$  and trigonal bipyramidal  $[\text{MnO}_5]$  units. A different pattern of planar honeycomb sheets are formed by edge-shared  $[\text{MnO}_6]$  octahedra, and these sublattices are connected through edge-shared dimers of  $[\text{MnO}_5]$  trigonal bipyramids to form corrugated sheets. Vanadate groups again condense the sheets into a three-dimensional framework. Infrared and Raman spectroscopies indicated the presence of OH groups and displayed characteristic Raman scattering due to vanadate groups. Temperature-dependent magnetic studies indicated Curie–Weiss behavior above 100 K with significant anti-ferromagnetic coupling for both compounds, with further complex magnetic behavior at lower temperatures. The data indicate canted anti-ferromagnetic order below 57 K in  $\text{Mn}_5(\text{VO}_4)_2(\text{OH})_4$  and below 45 K in  $\text{Mn}_6\text{O}(\text{VO}_4)_2(\text{OH})$ . Members of another class of compounds,  $\text{K}_2\text{M}_3(\text{VO}_4)_2(\text{OH})_2$  ( $M = \text{Mn}, \text{Co}$ ), also containing a honeycomb-type sublattice, were also synthesized to allow a comparison of the structural features across all three structure types and to demonstrate extension to other transition metals.



## 1. INTRODUCTION

The pentavalent vanadate unit ( $\text{VO}_4^{3-}$ ) is an excellent building block for a wide variety of metal complexes. The vanadium ion usually adopts a tetrahedral oxide environment and can serve in a wide variety of bridging arrangements creating chains, layers, and other complex solid structures.<sup>1–3</sup> In this way it can serve as a transition-metal surrogate for the extensive collection of metal phosphates. In addition, the vanadate can sometimes form oligomeric and polymeric groups, which further increase the structural options.<sup>4,5</sup> Though not producing a direct contribution to any magnetic signal, the vanadate tetrahedra can indirectly impart interesting magnetic behavior in materials by allowing magnetically active transition metals to assemble as low-dimensional structural features in a lattice. The rich structural behavior can include threefold clusters, chains, and layers and often leads to a variety of complex magnetic effects including spin frustration<sup>6–12</sup> and multiferroic behavior.<sup>13</sup> These resulting complex vanadates can exhibit bridging either directly through oxygen atoms ( $M\text{--O--M}$ ) or through the  $M\text{--O--V--O--M}$  linkage. In the latter case it can serve as a superexchange group (SSE)<sup>14,15</sup> and induce a reversal of the

usual Goodenough–Kanamori–Anderson exchange parameters.<sup>16</sup>

Our original interest in this area was driven by the performance of  $\text{YVO}_4$  as a laser host material, and we undertook an investigation of the hydrothermal synthesis of single crystals of the material.<sup>17</sup> This was successful,<sup>18,19</sup> but the development of the hydrothermal method also opened some considerably more complex chemistry of rare earth vanadates.<sup>20–22</sup> The rich trove of rare earth vanadate chemistry in hydrothermal fluids encouraged us to extend this chemistry to first-row transition-metal vanadates to provide a comparison to the results from more classical thermally driven synthesis methods. Indeed we found that the transition-metal vanadate chemistry is very extensive when using a high-temperature hydrothermal synthetic approach, and a wide variety of new compounds is emerging.<sup>23,24</sup> One particular advantage of this synthesis method is the tendency to form fairly large single crystals (1–2 mm). As a result, the method is particularly

Received: May 27, 2016

amenable for magnetically interesting materials, since single-crystal neutron and magnetism studies can be undertaken. The complex structures emerging in this area suggest that many new solid-state compounds await discovery. We continue to mine the area and explore the descriptive phase space by systematically varying reaction conditions. In this paper we describe several new manganese vanadates as high-quality single crystals with fairly complex structures, all representing different variations on a honeycomb-type lattice. Their structures are examined in detail, and their initial physical and magnetic properties are reported.

## 2. EXPERIMENTAL METHODS

**2.1. Hydrothermal Crystal Growth.** Compounds were synthesized using a high-temperature hydrothermal technique in sealed silver ampules. Approximately 0.2 g of reactants along with the desired aqueous mineralizer (~60% fill) were placed in 2.5 in. long silver ampules with an outer diameter of 1/4 in. The silver ampules were welded shut and placed in a Tuttle cold-seal style autoclave and filled with distilled water at 80% of free volume, to provide suitable counter pressure. The autoclave was heated to 580 °C for 7 d at a typical pressure of 1.5 kbar. The crystals were retrieved after washing with deionized water. The chemicals used in this study were used as received, without further purification:  $K_2CO_3$  (Alfa Aesar, 99.997%),  $Cs_2CO_3$  (Alfa Aesar, 99%),  $CsOH \cdot xH_2O$  (Alfa Aesar, 99.9%),  $CsCl$  (Alfa Aesar, 99.9%),  $Mn_2O_3$  (Alfa Aesar, 98%),  $Co_3O_4$  (Alfa Aesar, 99.7%), and  $V_2O_5$  (Alfa Aesar, 99.6%).

**2.2. Synthesis of  $K_2M_3(VO_4)_2(OH)_2$  ( $M = Mn$  and  $Co$ ).** Crystals of  $K_2Mn_3(VO_4)_2(OH)_2$  and  $K_2Co_3(VO_4)_2(OH)_2$  were isolated using 5 M KOH as the mineralizer. A total of 0.2 g of  $K_2CO_3$  (0.0578 g),  $Mn_2O_3$  (0.0661 g), and  $V_2O_5$  (0.0761 g) were mixed in a 1:1:1 molar ratio with 0.4 mL of 5 M KOH in each reaction. After the reaction period brown platelike crystals (Figure S1) were recovered (~70% of the total product), along with additional crystals of  $Mn(OH)_2$  and  $MnO$ . Similar reaction conditions were applied to synthesize  $K_2Co_3(VO_4)_2(OH)_2$ . Herein,  $Co_3O_4$  was used as the cobalt source. A lower yield of the target crystals was obtained (~10% of the total product), along with  $CoO$  powder.

**2.3. Synthesis of  $Mn_5(VO_4)_2(OH)_4$  and  $Mn_6O(VO_4)_3(OH)$ .** In a typical 7 d reaction, a mixture of  $Cs_2CO_3$  (0.0979 g),  $Mn_2O_3$  (0.0474 g), and  $V_2O_5$  (0.0547 g) was used in a molar ratio of 1:1:1 with the appropriate mineralizer. Dark red columnar crystals of  $Mn_5(VO_4)_2(OH)_4$  were obtained using 0.4 mL of 3 M CsOH as the mineralizer (Figure 1a). Alternatively, brown columnar crystals of

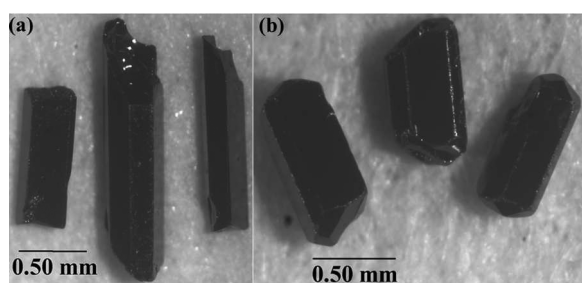


**Figure 1.** Hydrothermally grown crystals of  $Mn_5(VO_4)_2(OH)_4$  (a) and  $Mn_6O(VO_4)_3(OH)$  (b).

$Mn_6O(VO_4)_3(OH)$  were obtained using 0.4 mL of 1 M CsOH/3M CsCl as a mixed mineralizer (Figure 1b). In both cases, a minor amount (~5–10%) of  $Mn(OH)_2$  was observed as a side product.

**2.4. X-ray Diffraction.** Single-crystal X-ray intensity data of the title compounds were collected using a Rigaku AFC8 diffractometer with a  $Mo K\alpha$  ( $\lambda = 0.71073 \text{ \AA}$ ; graphite monochromated) sealed tube source and a Mercury CCD detector. Data were collected using  $\omega$ -scans with a width of 0.5 degrees. Data were processed and corrected

for absorption, Lorentz, and polarization effects using the CrystalClear software package.<sup>25</sup> Space group determinations were made based on the systematic absences. The structures were solved by direct methods and subsequently refined using full-matrix least-squares techniques within the SHELX software suite.<sup>26</sup> All non-hydrogen atoms were refined anisotropically. Initial structure refinements were considered with the infrared spectroscopic analysis (see below), and elemental analysis was completed by energy dispersive X-ray analysis (Supporting Information Table S1) and indicated that hydrogen atom identification was required to obtain appropriate charge balance. Bond valence analyses were used to confirm the divalent oxidation states of the transition metals and to identify underbonded oxygen atoms suitable for hydrogen atom assignment.<sup>27,28</sup> Hydrogen atoms were then identified from the difference electron density map and restrained to an appropriate distance from the parent oxygen atom. Crystallographic data from the refined structures is given in Table 1.

All powder XRD (PXRD) measurements were performed using a Rigaku Ultima IV diffractometer equipped with  $Cu K\alpha$  radiation of  $\lambda = 1.5406 \text{ \AA}$ .<sup>29</sup> Powder diffraction patterns were collected in  $0.02^\circ$  increments over the  $2\theta$  range of  $5^\circ$ – $65^\circ$  at a rate of  $0.1^\circ \text{ min}^{-1}$ . Comparisons of the observed and calculated PXRD patterns for hydrothermal reactions producing  $Mn_5(VO_4)_2(OH)_4$  and  $Mn_6O(VO_4)_3(OH)$  are shown in the Supporting Information, Figure S2.

**2.5. Magnetic Property Characterization.** Magnetization measurements were performed using a Magnetic Property Measurement System (Quantum Design) using collections of many small randomly oriented crystals of  $Mn_5(VO_4)_2(OH)_4$  and  $Mn_6O(VO_4)_3(OH)$  with total masses of 5.8 and 6.6 mg, respectively. Temperature-dependent measurements were conducted on cooling from 300 to 2 K in applied fields of 1 and 10 kOe. Isothermal magnetization curves were recorded upon decreasing the field from 50 kOe to zero at temperatures of 2 and 300 K.

**2.6. Spectroscopic Characterization.** Selected single crystals of  $Mn_5(VO_4)_2(OH)_4$  and  $Mn_6O(VO_4)_3(OH)$  were ground to powder form and used to perform the vibrational spectroscopic studies. To obtain infrared spectrum the ground single crystals were mixed and ground together with KBr before pressing into a pellet. The infrared spectra were collected using a Nicolet Magna IR Spectrometer 550 in the frequency range from 400 to  $4000 \text{ cm}^{-1}$  with a  $4 \text{ cm}^{-1}$  resolution. To obtain Raman scattering, the ground powders of single crystals were loaded into glass capillary holders. A 514.5 nm wavelength Ar laser (Innova 200, Coherent) was used with 90 mW to obtain the excitation of Raman scattering. Raman scattering was collected using a camera lens of  $f/1.2$  in a 1808 backscattering geometry and analyzed by a triple spectrometer (Tripletmate 1877, Spex) equipped with a charge-coupled device (CCD) detector (iDUS 420 series, Andor) cooled to 60 °C. A typical spectrum acquisition time was 10 s. The Raman spectrum of indine and the Raman spectrum of a 5:2 mixture of chloroform/bromoform was used for spectral calibration.

## 3. RESULTS AND DISCUSSION

**3.1. Synthesis and Phase Stability.** The synthetic approach for single crystals of the title compounds was drawn from recent synthesis of other transition-metal vanadates possessing low-dimensional structural features.<sup>23,24</sup> As a general approach, those studies involved the hydrothermal reactions of varying stoichiometries of AEO ( $AE = Sr, Ba$ ) with  $M_2O_3$  ( $M = V, Mn, Fe$ ) and  $V_2O_5$  in alkali hydroxide mineralizers. In the resulting structures,  $Sr^{2+}$  or  $Ba^{2+}$  cations were present as a primary structural building block. In the present study, such alkaline earth metal components were absent from the reaction, leading to different chemistry. By varying the mineralizer between KOH, CsOH, and CsCl we observed the three different products  $K_2M_3(VO_4)_2(OH)_2$  ( $M = Mn, Co$ ),  $Mn_5(VO_4)_2(OH)_4$ , and  $Mn_6O(VO_4)_3(OH)$ , respectively. Despite the presence of excess Cs in the synthesis reactions of the latter compounds no Cs-containing product was observed. Here, the  $Cs^+$  ions strictly served as mineralizing counterions

Table 1. Crystallographic Data for  $K_2Mn_3(VO_4)_2(OH)_2$ ,  $Mn_5(VO_4)_2(OH)_4$ , and  $Mn_6O(VO_4)_3(OH)$ 

empirical formula	$K_2Mn_3(VO_4)_2(OH)_2$	$Mn_5(VO_4)_2(OH)_4$	$Mn_6O(VO_4)_3(OH)$
FW	506.92	572.61	707.47
crystal system	monoclinic	monoclinic	monoclinic
crystal dimension, mm	$0.28 \times 0.16 \times 0.14$	$0.18 \times 0.06 \times 0.04$	$0.12 \times 0.03 \times 0.02$
space group, Z	$C2/m$ (No. 12), 2	$C2/m$ (No. 12), 2	$P2_1/m$ (No. 11), 2
T, °C	25	25	25
a, Å	15.184(5)	9.6568(9)	8.9363(12)
b, Å	6.1578(19)	9.5627(9)	6.4678(8)
c, Å	5.3916(19)	5.4139(6)	10.4478(13)
$\beta$ , deg	105.326(9)	98.529(8)	99.798(3)
V, Å <sup>3</sup>	486.2(3)	494.42(9)	595.06(13)
D(calc), Mg/m <sup>3</sup>	3.463	3.846	3.948
$\mu$ (Mo K $\alpha$ ), mm <sup>-1</sup>	6.535	8.047	8.462
Tmin	0.6801	0.7894	0.5741
Tmax	1.0000	1.0000	1.0000
2 $\theta$ range	3.59–25.04	3.01–25.24	2.31–25.24
No. of reflns.	2061	2128	5127
unique reflns.	488	475	1168
observed reflns. ( $I > 2\sigma(I)$ )	479	448	1110
R(int)	0.0285	0.0261	0.0467
No. of parameters	53	54	131
final R [ $I > 2\sigma(I)$ ] R1, wR2	0.0279/0.0680	0.0426/0.0988	0.0321/0.0815
final R (all data) R1, wR2	0.0282/0.0683	0.0441/0.1018	0.0335/0.832
GOF	1.154	1.147	1.144
largest diff. peak/hole, e/Å <sup>3</sup>	0.879/−0.773	1.152/−2.396	1.051/−0.941

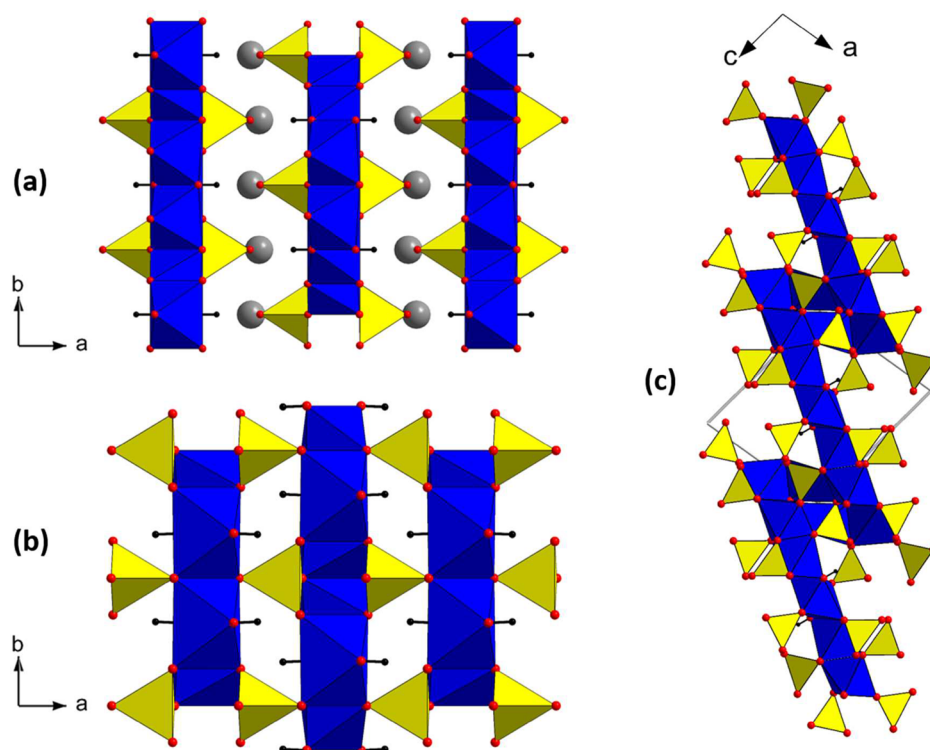


**Figure 2.** Long-range structural comparison of (a)  $K_2Mn_3(VO_4)_2(OH)_2$ , (b)  $Mn_5(VO_4)_2(OH)_4$ , and (c)  $Mn_6O(VO_4)_3(OH)$ . Manganese and vanadium are depicted as blue and yellow polyhedra, respectively. Oxygen atoms are shown as red spheres, potassium atoms as gray spheres, and hydrogen atoms as black spheres.

and remained in solution. Both compounds contain transition-metal ions that were reduced from their initial trivalent state in the feedstock material to a divalent state in the resulting crystals. Note that  $Mn_5(VO_4)_2(OH)_4$  is actually a stoichiometric form of the very rare arsenic-substituted mineral

reppiaite,  $Mn_5(V_{0.89}As_{0.11})_2(OH)_4$ .<sup>30</sup> In addition, the structure of  $K_2Mn_3(VO_4)_2(OH)_2$  has been briefly reported as made by a high-temperature melt reaction,<sup>31</sup> but to our knowledge there have been no follow-up reports. No chemistry of any other similar compounds has been reported, nor have any physical

properties been determined. Thus, a brief comparison of these structures is instructive both in regard to the preparation of other transition-metal analogues (such as  $\text{K}_2\text{Co}_3(\text{VO}_4)_2(\text{OH})_2$  in the present study, Supporting Information Table S2) and for a direct structural comparison of the structural relationships between  $\text{K}_2\text{Mn}_3(\text{VO}_4)_2(\text{OH})_2$ ,  $\text{Mn}_5(\text{VO}_4)_2(\text{OH})_4$ , and  $\text{Mn}_6\text{O}(\text{VO}_4)_3(\text{OH})$  to provide a broader understanding of transition-metal vanadate crystal chemistry.

**3.2. Structural Relationships in  $\text{K}_2\text{Mn}_3(\text{VO}_4)_2(\text{OH})_2$ ,  $\text{Mn}_5(\text{VO}_4)_2(\text{OH})_4$ , and  $\text{Mn}_6\text{O}(\text{VO}_4)_2(\text{OH})$ .** We will first briefly describe each structure and then examine some interesting relationships between them, using the Mn-containing compounds as the representative examples for ease of comparison. The structure of  $\text{K}_2\text{Mn}_3(\text{VO}_4)_2(\text{OH})_2$  (and the analogous Co species) can be described as alternating layers of transition-metal vanadates with potassium ions (Figure 2a). The transition-metal vanadate layer consists of two unique  $[\text{MnO}_6]$  octahedra (both in the form of  $\text{MnO}_4(\text{OH})_2$ , where the oxo groups are from the vanadates) and one unique  $[\text{VO}_4]$  tetrahedron. The  $[\text{MnO}_6]$  units form a sheet in the  $bc$  plane via shared oxygen edges, and the  $[\text{VO}_4]$  units extend from this sheet along the  $a$ -axis. The sheets are completely isolated from one another by layers of potassium ions, which satisfy the remainder of the valence of the vanadate-bound oxygen atoms. These sheets of edge-shared  $[\text{MnO}_6]$  units form a honeycomb-like arrangement in the  $bc$  plane that will be described in greater detail below as it relates to similar features in  $\text{Mn}_5(\text{VO}_4)_2(\text{OH})_4$  and  $\text{Mn}_6\text{O}(\text{VO}_4)_2(\text{OH})$ .

The key structural feature of  $\text{Mn}_5(\text{VO}_4)_2(\text{OH})_4$  is again marked by a two-dimensional transition-metal sheet in the  $bc$  plane, but here the sheets are condensed through the vanadate tetrahedra extending along the  $a$ -axis (Figure 2b). The absence of an alkali metal layer in this structure requires that the vanadate oxygen atoms satisfy their valence in some other way, namely, by connecting to the next transition-metal oxide layer. Overall, the  $\text{Mn}_5(\text{VO}_4)_2(\text{OH})_4$  structure is considered a three-dimensional transition-metal vanadate framework, but it retains the two-dimensional character with respect to the manganese oxide network. Similar condensation of manganese oxide layers occurs between zigzag layers through the orthovanadate groups in  $\text{Mn}_3(\text{VO}_4)_2$ .<sup>32</sup> Connectivity of distorted octahedral  $[\text{MnO}_6]$  units (as  $[\text{MnO}_4(\text{OH})_2]$  and  $[\text{MnO}_2(\text{OH})_4]$ ) within the layers again occurs via edge-sharing but forms a different honeycomb arrangement than that of  $\text{K}_2\text{Mn}_3(\text{VO}_4)_2(\text{OH})_2$  (see below). Interestingly,  $\text{K}_2\text{Mn}_3(\text{VO}_4)_2(\text{OH})_2$  and  $\text{Mn}_5(\text{VO}_4)_2(\text{OH})_4$  share certain similarities in that they are both based on a two-dimensional transition-metal oxide sheet, but they are quite distinct in the nature and connectivity of the sheets due to the presence/absence of the alkali metal as well as the Mn/V ratio in their formulas. This marks the first fundamental structural distinction between  $\text{K}_2\text{Mn}_3(\text{VO}_4)_2(\text{OH})_2$  and  $\text{Mn}_5(\text{VO}_4)_2(\text{OH})_4$ . The stoichiometric distinction is especially apparent when comparing the unit cell projections along their respective  $a$ -axes (Figure 3).

The structure of  $\text{Mn}_6\text{O}(\text{VO}_4)_3(\text{OH})$  differs somewhat from these first two structure types (Figure 2c). Two-dimensional manganese oxide layers are again observed to connect through vanadate groups to form a three-dimensional manganese vanadate framework as in  $\text{Mn}_5(\text{VO}_4)_2(\text{OH})_4$ . In this case however the structure is considerably more complicated in its construction. One difference is that the  $\text{Mn}_6\text{O}(\text{VO}_4)_3(\text{OH})$  structure contains five unique Mn atoms that are either five- or six-coordinate, accounting for four different Mn(II) coordina-

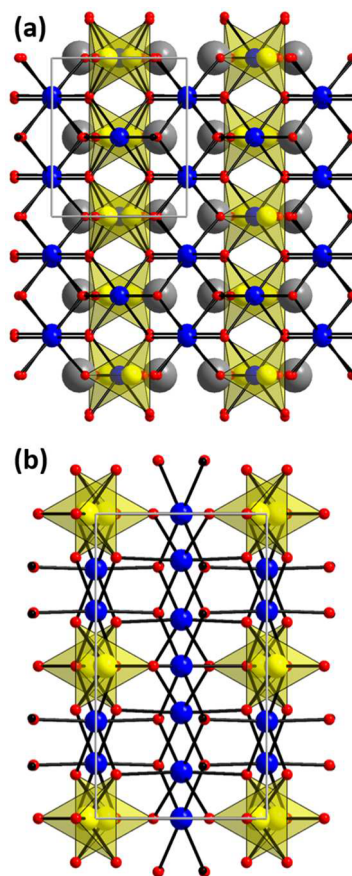


**Figure 3.** Projection of  $\text{K}_2\text{Mn}_3(\text{VO}_4)_2(\text{OH})_2$  (a) and  $\text{Mn}_5(\text{VO}_4)_2(\text{OH})_4$  (b) along  $[100]$ . C-centering places the individual layers in a staggered arrangement relative to one another along the  $a$ -axis.

tion environments as  $[\text{MnO}_5]$ ,  $[\text{MnO}_6]$ ,  $[\text{MnO}_5(\text{OH})]$ , and  $[\text{MnO}_4(\text{OH})_2]$ . The six-coordinate Mn atoms (Mn(2), Mn(3), and Mn(4)) are edge-sharing to form a planar substructure that contains the honeycomb-like feature (discussed below). This substructure can be thought of as resembling a Kagome strip lattice,<sup>33</sup> with three chains (propagating by oxygen edge sharing along the  $b$ -axis) of the six-coordinate Mn(4), Mn(3), and Mn(4) units that are linked by Mn(2), again by oxygen edge-sharing to form discrete planar subsheets (Figure 4). The planar substructures are then connected to one another through  $[\text{Mn}_2\text{O}_8]$  dimers of the trigonal bipyramidal  $[\text{MnO}_5]$  units Mn(1) and Mn(5), by both edge and corner sharing (Figure 5). The result is a corrugated manganese oxide sheet that approximately bisects the  $ac$  plane (Figure 2c). This sheet is heavily decorated by vanadate tetrahedra, which provide connectivity to the neighboring corrugated sheets aligned in an interlocking manner.

These basic structural observations may provide some insight into the descriptive chemistry observed. When  $\text{K}^+$  ions are employed in the synthesis the alkali ions become incorporated between the layers as part of the structural unit. When the mineralizer contains cesium, we may postulate that the  $\text{K}_2\text{Mn}_3(\text{VO}_4)_2(\text{OH})_2$  structure type may not be stable due to the larger size of the  $\text{Cs}^+$  cation, where the reactions instead produce  $\text{Mn}_5(\text{VO}_4)_2(\text{OH})_4$  or  $\text{Mn}_6\text{O}(\text{VO}_4)_3(\text{OH})$ . Alternatively, the  $\text{Cs}^+$  ions may be more stable as solvated aquo ions and prefer to remain in solution rather than the lattice. The role

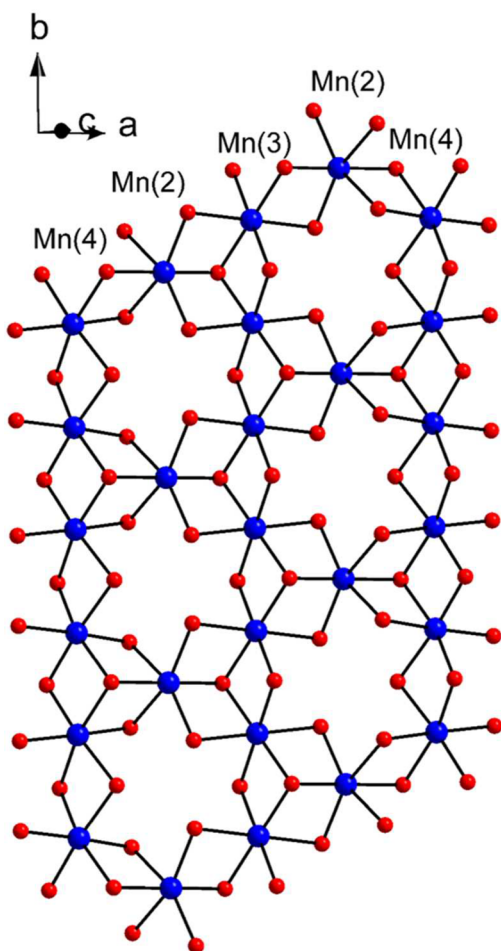


**Figure 4.** Planar manganese oxide substructure of  $\text{Mn}_6\text{O}(\text{VO}_4)_3(\text{OH})$  comprised of edge-sharing  $[\text{MnO}_6]$  units.

of the alkali metal as a structural spacer is also evident, in that the manganese vanadate layers are isolated from one another in  $\text{K}_2\text{Mn}_3(\text{VO}_4)_2(\text{OH})_2$ . When an alkali metal ion is not present, the manganese oxide networks remain two-dimensional in  $\text{Mn}_5(\text{VO}_4)_2(\text{OH})_4$  and  $\text{Mn}_6\text{O}(\text{VO}_4)_3(\text{OH})$  but are condensed through the vanadate tetrahedra. An interesting crystal chemical comparison is found in  $\text{Mn}_2(\text{VO}_4)(\text{OH})$ ,<sup>34</sup> where the presence of both trigonal bipyramidal and octahedral Mn environments results in a corrugated layer structure, similar to  $\text{Mn}_6\text{O}(\text{VO}_4)_3(\text{OH})$  that also contains both types of building blocks. The layers in  $\text{Mn}_2(\text{VO}_4)(\text{OH})$  are also similarly condensed through the vanadate groups. Typical Mn(II)–O bond lengths were observed in all of the structures in this study (Table 2, Table S3).

The six-coordinate  $[\text{MnO}_6]$  units of  $\text{K}_2\text{Mn}_3(\text{VO}_4)_2(\text{OH})_2$ ,  $\text{Mn}_5(\text{VO}_4)_2(\text{OH})_4$  and  $\text{Mn}_6\text{O}(\text{VO}_4)_3(\text{OH})$  possess average Mn–O distances of 2.188(3), 2.205(4), and 2.208(3) Å occurring over ranges from 2.098(3) to 2.245(2), from 2.087(3) to 2.271(3), and from 2.059(2) to 2.472(3) Å, respectively. In general, Mn–O bonds to  $\mu_3$ -oxo vertices correspond to the shortest bonds in those ranges (excepting O(1) in  $\text{Mn}_5(\text{VO}_4)_2(\text{OH})_4$ , where O(1) is held at a longer distance from Mn by the bridging vanadate group). The resulting Mn–O–Mn bond angles for the edge-sharing connections of  $[\text{MnO}_6]$  groups range from 83.51(10)° to 99.32(11)° in  $\text{K}_2\text{Mn}_3(\text{VO}_4)_2(\text{OH})_2$ , from 84.75(14)° to 101.70(14)° in  $\text{Mn}_5(\text{VO}_4)_2(\text{OH})_4$ , and from 87.37(8)° to

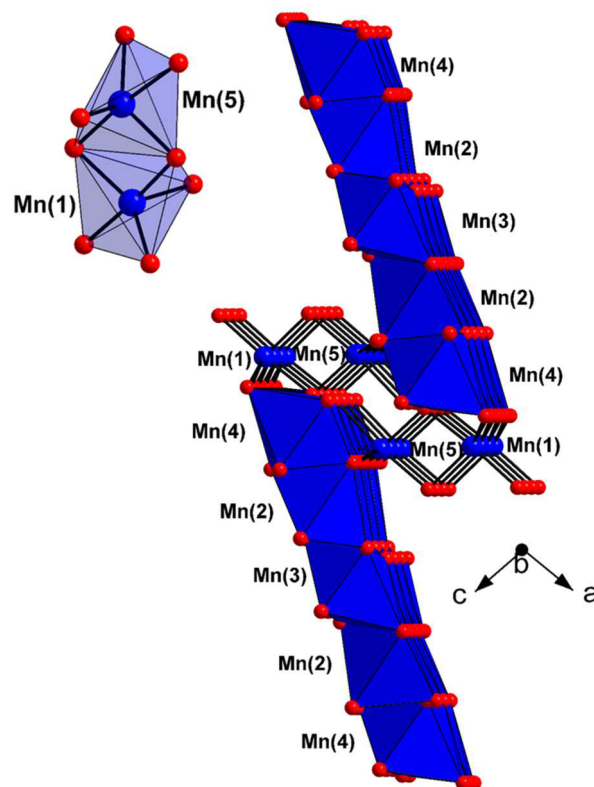


**Figure 5.** Perspective view of the structural connectivity of planar  $\text{MnO}_6$ -based units (shown as polyhedra) through  $\text{MnO}_5$ -based  $[\text{Mn}_2\text{O}_8]$  dimers. (inset) Edge-sharing connectivity within the dimers.

102.39(15)° in  $\text{Mn}_6\text{O}(\text{VO}_4)_3(\text{OH})$ . As an additional note on the interatomic relationships in  $[\text{MnO}_6]$  units, the longer Mn(2)–O(9) bonds of 2.472(3) Å in  $\text{Mn}_6\text{O}(\text{VO}_4)_3(\text{OH})$  indicate a high degree of distortion about the  $[\text{Mn}(2)\text{O}_6]$  octahedron, where such long bonds are necessary to mitigate the acute O(9)–Mn(2)–O(9) bond angle of 66.17(12)°. The Mn–O bond lengths of the  $[\text{MnO}_5]$  groups in  $\text{Mn}_6\text{O}(\text{VO}_4)_3(\text{OH})$  range from 2.021(4) to 2.261(3) Å, with an average of 2.118(4) Å. The  $\text{Co}^{2+}$  analogue to  $\text{K}_2\text{Mn}_3(\text{VO}_4)_2(\text{OH})$  exhibits similar trends in its interatomic distances and angles (Table S2), with correspondingly shorter values, as expected based on the Shannon radii.<sup>35</sup> In all cases the V–O bond lengths all fall within the range from 1.665(4) to 1.787(4) Å, typical for  $\text{V}^{5+}$ .<sup>35</sup>

**3.3. Honeycomb Variations in  $\text{K}_2\text{Mn}_3(\text{VO}_4)_2(\text{OH})_2$ ,  $\text{Mn}_5(\text{VO}_4)_2(\text{OH})_4$ , and  $\text{Mn}_6\text{O}(\text{VO}_4)_2(\text{OH})$ .** All three compounds highlighted here contain triangular  $[\text{Mn}_3\text{O}_{13}]$  building blocks that are responsible for constructing the two-dimensional manganese oxide networks. This recurring pattern is worthy of further structural comment, especially since it could represent a potential magnetically frustrated system with a pattern of honeycomb-like hexagons.<sup>36</sup> The prototype  $[\text{Mn}_3\text{O}_{13}]$  triangular unit was originally observed in  $\text{K}_2\text{Mn}_3(\text{VO}_4)_2(\text{OH})_2$ ,<sup>31</sup> and the present study demonstrates its application to other transition metals such as  $\text{Co}^{2+}$ . This also provides an interesting comparison point between  $\text{K}_2\text{Mn}_3(\text{VO}_4)_2(\text{OH})_2$ ,  $\text{Mn}_5(\text{VO}_4)_2(\text{OH})_4$ , and  $\text{Mn}_6\text{O}(\text{VO}_4)_2(\text{OH})$ .

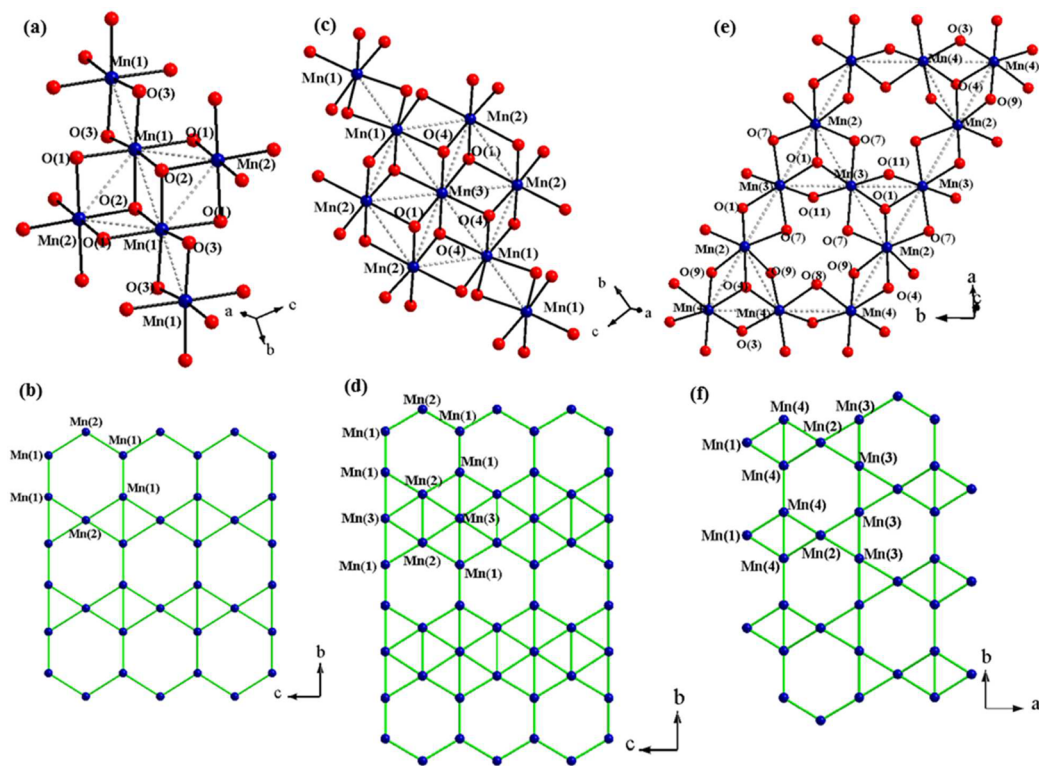
The edge-sharing  $[\text{MnO}_6]$  octahedra in  $\text{K}_2\text{Mn}_3(\text{VO}_4)_2(\text{OH})_2$  and  $\text{Mn}_5(\text{VO}_4)_2(\text{OH})_4$  form triangular Mn–Mn interactions ( $[\text{Mn}_3\text{O}_{13}]$  triangular units) alternating along [010] (Figure

Table 2. Selected Interatomic Distances (Å) and Angles (deg) for  $\text{Mn}_5(\text{VO}_4)_2(\text{OH})_4$  and  $\text{Mn}_6\text{O}(\text{VO}_4)_3(\text{OH})$ 

$\text{Mn}_5(\text{VO}_4)_2(\text{OH})_4$					
	$\text{Mn}(1)\text{O}_6$			$\text{Mn}(3)\text{O}_6$	
$\text{Mn}(1)-\text{O}(2) \times 2$		2.269(3)	$\text{Mn}(3)-\text{O}(1) \times 2$		2.253(4)
$\text{Mn}(1)-\text{O}(3) \times 2$		2.175(3)	$\text{Mn}(3)-\text{O}(2) \times 4$		2.150(3)
$\text{Mn}(1)-\text{O}(4) \times 2$		2.126(3)			
	$\text{Mn}(2)\text{O}_6$			$\text{V}(1)\text{O}_4$	
$\text{Mn}(2)-\text{O}(1) \times 2$		2.270(3)	$\text{V}(1)-\text{O}(1)$		1.748(4)
$\text{Mn}(2)-\text{O}(2) \times 2$		2.259(3)	$\text{V}(1)-\text{O}(2) \times 2$		1.708(3)
$\text{Mn}(2)-\text{O}(4) \times 2$		2.087(3)	$\text{V}(1)-\text{O}(3)$		1.722(4)
$\text{Mn}(1)\cdots\text{Mn}(1)$		2.9312(17)	$\text{Mn}(1)-\text{O}(3)-\text{Mn}(1)$		84.75(14)
$\text{Mn}(1)\cdots\text{Mn}(2)$		3.1362(5)	$\text{Mn}(1)-\text{O}(2)-\text{Mn}(2)$		87.69(10)
$\text{Mn}(1)\cdots\text{Mn}(3)$		3.3158(9)	$\text{Mn}(1)-\text{O}(4)-\text{Mn}(2)$		96.23(12)
$\text{Mn}(2)\cdots\text{Mn}(2)$		3.4642(15)	$\text{Mn}(1)-\text{O}(4)-\text{Mn}(3)$		101.70(14)
$\text{Mn}(2)\cdots\text{Mn}(3)$		3.2137(5)	$\text{Mn}(2)-\text{O}(1)-\text{Mn}(2)$		99.44(17)
			$\text{Mn}(2)-\text{O}(1)-\text{Mn}(3)$		90.55(12)
			$\text{Mn}(2)-\text{O}(4)-\text{Mn}(3)$		98.67(12)
$\text{Mn}_6\text{O}(\text{VO}_4)_3(\text{OH})$					
	$\text{Mn}(1)\text{O}_5$			$\text{Mn}(5)\text{O}_5$	
$\text{Mn}(1)-\text{O}(3)$		2.082(4)	$\text{Mn}(5)-\text{O}(2)$		2.261(3)
$\text{Mn}(1)-\text{O}(5) \times 2$		2.151(3)	$\text{Mn}(5)-\text{O}(3)$		2.021(4)
$\text{Mn}(1)-\text{O}(6)$		2.102(4)	$\text{Mn}(5)-\text{O}(6)$		2.123(4)
$\text{Mn}(1)-\text{O}(10)$		2.087(4)	$\text{Mn}(5)-\text{O}(9) \times 2$		2.097(2)
	$\text{Mn}(2)\text{O}_6$			$\text{V}(1)\text{O}_4$	
$\text{Mn}(2)-\text{O}(1)$		2.116(4)	$\text{V}(1)-\text{O}(5) \times 2$		1.708(2)
$\text{Mn}(2)-\text{O}(4)$		2.106(3)	$\text{V}(1)-\text{O}(6)$		1.691(4)
$\text{Mn}(2)-\text{O}(7) \times 2$		2.136(3)	$\text{V}(1)-\text{O}(11)$		1.699(4)
$\text{Mn}(2)-\text{O}(9) \times 2$		2.472(3)		$\text{V}(2)\text{O}_4$	
	$\text{Mn}(3)\text{O}_6$		$\text{V}(2)-\text{O}(4)$		1.787(4)
$\text{Mn}(3)-\text{O}(1) \times 2$		2.118(2)	$\text{V}(2)-\text{O}(7) \times 2$		1.696(3)
$\text{Mn}(3)-\text{O}(7) \times 2$		2.320(3)	$\text{V}(2)-\text{O}(8)$		1.728(4)
$\text{Mn}(3)-\text{O}(11) \times 2$		2.127(2)		$\text{V}(3)\text{O}_4$	
	$\text{Mn}(4)\text{O}_6$		$\text{V}(3)-\text{O}(2)$		1.753(4)
$\text{Mn}(4)-\text{O}(2)$		2.252(2)	$\text{V}(3)-\text{O}(9) \times 2$		1.738(3)
$\text{Mn}(4)-\text{O}(3)$		2.059(2)	$\text{V}(3)-\text{O}(10)$		1.665(4)
$\text{Mn}(4)-\text{O}(4)$		2.275(3)			
$\text{Mn}(4)-\text{O}(5)$		2.144(2)	$\text{Mn}(1)-\text{O}(3)-\text{Mn}(4)$		98.16(12)
$\text{Mn}(4)-\text{O}(8)$		2.184(2)	$\text{Mn}(1)-\text{O}(5)-\text{Mn}(4)$		93.56(10)
$\text{Mn}(4)-\text{O}(9)$		2.288(2)	$\text{Mn}(1)-\text{O}(3)-\text{Mn}(5)$		98.60(15)
			$\text{Mn}(1)-\text{O}(6)-\text{Mn}(3)$		94.84(15)
$\text{Mn}(1)\cdots\text{Mn}(4)$		3.1296(8)	$\text{Mn}(2)-\text{O}(1)-\text{Mn}(3)$		99.42(12)
$\text{Mn}(1)\cdots\text{Mn}(5)$		3.1112(11)	$\text{Mn}(2)-\text{O}(7)-\text{Mn}(3)$		92.79(10)
$\text{Mn}(2)\cdots\text{Mn}(3)$		3.2296(7)	$\text{Mn}(2)-\text{O}(4)-\text{Mn}(4)$		97.31(12)
$\text{Mn}(3)\cdots\text{Mn}(3)$		3.2339(4)	$\text{Mn}(2)-\text{O}(9)-\text{Mn}(4)$		87.37(8)
$\text{Mn}(4)\cdots\text{Mn}(4)$		3.2092(10)	$\text{Mn}(3)-\text{O}(1)-\text{Mn}(3)$		99.55(14)
			$\text{Mn}(3)-\text{O}(11)-\text{Mn}(3)$		98.98(15)
			$\text{Mn}(4)-\text{O}(2)-\text{Mn}(4)$		92.69(13)
			$\text{Mn}(4)-\text{O}(3)-\text{Mn}(4)$		102.39(15)
			$\text{Mn}(4)-\text{O}(4)-\text{Mn}(4)$		89.69(13)
			$\text{Mn}(4)-\text{O}(8)-\text{Mn}(4)$		96.49(14)
			$\text{Mn}(4)-\text{O}(2)-\text{Mn}(5)$		93.22(11)
			$\text{Mn}(4)-\text{O}(9)-\text{Mn}(5)$		96.71(10)

6a). In  $\text{K}_2\text{Mn}_3(\text{VO}_4)_2(\text{OH})_2$ , these  $[\text{Mn}_3\text{O}_{13}]$  triangular units are comprised of two  $[\text{Mn}(1)\text{O}_6]$  and one  $[\text{Mn}(2)\text{O}_6]$  octahedra connected through shared oxygen edges to form one central  $\mu_3$ -oxygen atom, O(2), which is the  $\text{OH}^-$  group in the structure. Consequently, the arrangement of  $[\text{Mn}_3\text{O}_{13}]$  units in  $\text{K}_2\text{Mn}_3(\text{VO}_4)_2(\text{OH})_2$  create honeycomb-like Mn hexagons (Figure 6b) in a shifted kagome arrangement. In contrast to  $\text{K}_2\text{Mn}_3(\text{VO}_4)_2(\text{OH})_2$ ,  $\text{Mn}_5(\text{VO}_4)_2(\text{OH})_4$  contains two unique triangular  $[\text{Mn}_3\text{O}_{13}]$  units formed by the presence

of the additional Mn atom (labeled Mn(3)) in the sheets (Figure 6c). One triangle is made of two  $[\text{Mn}(2)\text{O}_6]$  units and one  $[\text{Mn}(3)\text{O}_6]$  unit sharing O(1) as a  $\mu_3$ -oxo vertex, while the other triangle is made from  $[\text{Mn}(1)\text{O}_6]$ ,  $[\text{Mn}(2)\text{O}_6]$ , and  $[\text{Mn}(3)\text{O}_6]$  octahedra sharing O(4) as a  $\mu_3$ -oxygen atom. In this case O(4) is the  $\text{OH}^-$  group in the structure, while O(1) maintains an additional bond to the vanadium atom that connects the sheets along the *a*-axis. The Mn–Mn sheets in  $\text{Mn}_5(\text{VO}_4)_2(\text{OH})_4$  also consists of honeycomb-like Mn



**Figure 6.** Comparison of partial structure of Mn–O honeycomb sublattices in  $\text{K}_2\text{Mn}_3(\text{VO}_4)_2(\text{OH})_2$  (a),  $\text{Mn}_5(\text{VO}_4)_2(\text{OH})_4$  (c) and  $\text{Mn}_6\text{O}(\text{VO}_4)_3(\text{OH})$  (e). The unique feature of these compounds are the triangular  $[\text{Mn}_3\text{O}_{13}]$  units connect to form a layers of Mn–Mn hexagons as shown in green lines in (b, d, and f). The green lines represent a shared oxygen edge between Mn atoms.

hexagons (similar to  $\text{K}_2\text{Mn}_3(\text{VO}_4)_2(\text{OH})_2$ ) but alternating with three rows of triangular Mn atoms along  $[010]$  (Figure 6d). Effectively, this latter arrangement is a hexagonal honeycomb lattice where every other row of hexagons has an additional Mn atom in the center of each Mn hexagon, creating the triangular rows. This difference may be the manifestation of the different Mn/V stoichiometries in the chemical formulas of  $\text{K}_2\text{Mn}_3(\text{VO}_4)_2(\text{OH})_2$  and  $\text{Mn}_5(\text{VO}_4)_2(\text{OH})_4$ , where the latter structure, being richer in Mn, forms the more complicated sheet.

The planar honeycomb substructure formed by  $[\text{Mn}_3\text{O}_{13}]$  units in  $\text{Mn}_6\text{O}(\text{VO}_4)_3(\text{OH})$  (Figure 6e) is a variation on the infinite planar structure of  $\text{K}_2\text{Mn}_3(\text{VO}_4)_2(\text{OH})_2$  in that the hexagons formed by the edge-sharing Mn atoms are staggered along  $[010]$  relative to one another (Figure 6f). There are two unique  $[\text{Mn}_3\text{O}_{13}]$  units in the structure, one comprised of one  $[\text{Mn}(2)\text{O}_6]$  unit and two  $[\text{Mn}(3)\text{O}_6]$  units sharing O(1) as a  $\mu_3$ -oxo vertex, and the other comprised of one  $[\text{Mn}(2)\text{O}_6]$  unit with two  $[\text{Mn}(4)\text{O}_6]$  units with O(4) as the  $\mu_3$ -oxo atom. Here, O(1) is an OH<sup>−</sup> group, while O(4) is further bound to a vanadium atom. This arrangement creates somewhat more open layers compared to  $\text{K}_2\text{Mn}_3(\text{VO}_4)_2(\text{OH})_2$  and  $\text{Mn}_5(\text{VO}_4)_2(\text{OH})_4$ . As these planar honeycomb units are connected to form the corrugated sheet by the  $[\text{Mn}_2\text{O}_8]$  dimers, the trigonal bipyramidal Mn(1) atom also occurs in the same plane with the octahedral Mn(2), Mn(3), and Mn(4) atoms. This adds additional complexity to the triangular system by the formation of an oxygen edge-sharing triangular  $[\text{Mn}_3\text{O}_{12}]$  unit in the same plane from one  $[\text{Mn}(1)\text{O}_5]$  and two  $[\text{Mn}(4)\text{O}_6]$  units, with O(3) serving as the  $\mu_3$ -oxo vertex. The O(3) atom also coordinates Mn(5) outside of the plane, as

the  $[\text{Mn}_2\text{O}_8]$  dimer is formed by a shared O(3)–O(6) edge of Mn(1) and Mn(5).

**3.4. Magnetic Properties of  $\text{Mn}_5(\text{VO}_4)_2(\text{OH})_4$  and  $\text{Mn}_6\text{O}(\text{VO}_4)_3(\text{OH})$ .** Both  $\text{Mn}_5(\text{VO}_4)_2(\text{OH})_4$  and  $\text{Mn}_6\text{O}(\text{VO}_4)_3(\text{OH})$  possess very complicated Mn–O–Mn networks. The generally low symmetry of the systems gives rise to  $[\text{MnO}_6]$  units that are distorted to different degrees with wide ranges of Mn–O–Mn bond angles and Mn⋯O⋯Mn separation distances. The presence of very different  $[\text{MnO}_5]$  and  $[\text{MnO}_6]$  geometries in  $\text{Mn}_6\text{O}(\text{VO}_4)_3(\text{OH})$  introduces additional variables. Given the diversity of bond distances and angles, multiple superexchange pathways and, thus, complex magnetic interactions, are possible. In that way, the structures of both  $\text{Mn}_5(\text{VO}_4)_2(\text{OH})_4$  and  $\text{Mn}_6\text{O}(\text{VO}_4)_3(\text{OH})$  are fairly complex, making straightforward interpretation of magnetic properties somewhat difficult.

The measured magnetic properties of  $\text{Mn}_5(\text{VO}_4)_2(\text{OH})_4$  are summarized in Figure 7. The temperature dependence of the  $M/H$  (the magnetic susceptibility when  $M$  vs  $H$  is linear) is shown in Figure 7a. The Figure 7a inset shows the inverse,  $H/M$ . The Curie–Weiss relationship  $M/H = C/(T - \theta)$  is observed to hold for temperatures above  $\sim 100$  K, and a fit over this temperature range is shown in the inset. This gives an effective moment of  $5.69 \mu_{\text{B}}/\text{Mn}$ , which is close to, but slightly smaller than, the expected free ion value of  $5.9 \mu_{\text{B}}/\text{Mn}^{2+}$  ( $S = 5/2$ ). The Weiss temperature  $\theta$  is found to be  $-164$  K, indicating relatively strong, predominantly anti-ferromagnetic interactions between the  $\text{Mn}^{2+}$  moments. An anomaly is observed at  $\sim 57$  K, which is most easily seen at lower fields. The field dependence of the magnetic moment (Figure 7b) is nearly linear both above and below this temperature, indicating the anomaly at 57 K most likely corresponds to anti-

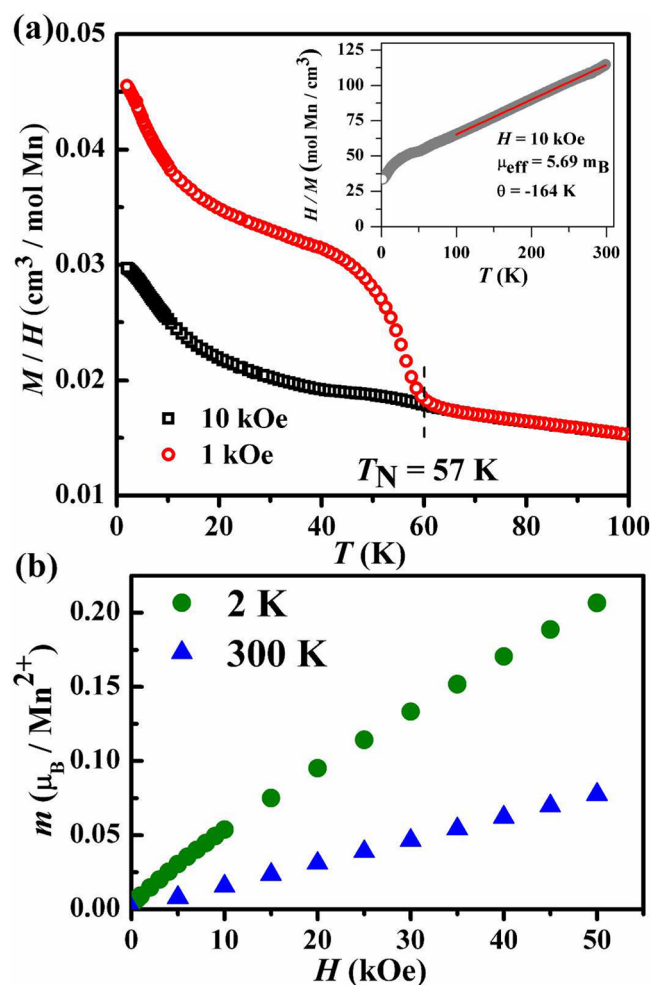


**Figure 7.** Magnetic properties of  $\text{Mn}_5(\text{VO}_4)_2(\text{OH})_4$ . (a) Temperature dependence of  $M/H$  measured in applied fields of  $H = 1$  and  $10$  kOe. (inset)  $H/M$  with a Curie–Weiss fit between  $100$  and  $300$  K. (b) Magnetic moment vs applied field measured at  $2$  and  $300$  K.

ferromagnetic order, so this temperature is defined as the Neel temperature  $T_N$ . The increase in  $M/H$  below this temperature seen at  $H = 1$  kOe suggests the moments are canted, producing a small net moment in the ordered state. Below  $\sim 20$  K,  $M/H$  displays an additional increase upon cooling, with Curie-like behavior. This most likely arises from magnetic moments that do not undergo magnetic order at  $T_N$  and remain paramagnetic to  $2$  K, which might be expected based on the frustrated lattice formed by  $\text{Mn}^{2+}$ . There is a slight rollover of  $M/H$  observed near the lowest temperature studied here, indicating that the magnetic structure may still be evolving with temperature at  $2$  K and below.

**Figure 8** shows the magnetic properties of  $\text{Mn}_6\text{O}(\text{VO}_4)_3(\text{OH})$ . The temperature dependence (**Figure 8a**) is described by a Curie–Weiss law above  $100$  K, with an effective moment of  $5.4 \mu_B/\text{Mn}$ . As observed in  $\text{Mn}_5(\text{VO}_4)_2(\text{OH})_4$ , this is somewhat smaller than the expected value. The negative Weiss temperature of  $-113$  K indicates predominantly anti-ferromagnetic interactions in this compound as well. Evidence for long-range order is seen at  $\sim 45$  K. Below this temperature the magnetization increases sharply, and a portion of the moment saturates at low magnetic field at  $2$  K (**Figure 8c**). The saturating component of the moment is small,  $\sim 0.03$  mB/Mn, consistent with a canted anti-ferromagnetic structure with

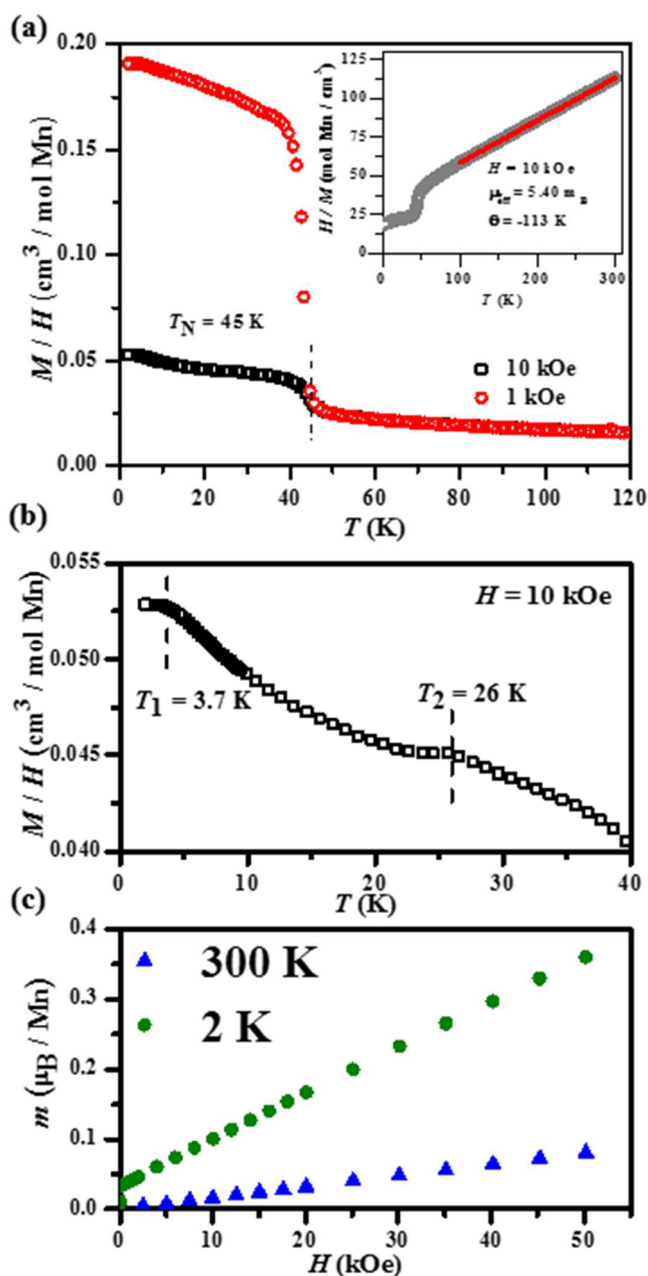


**Figure 8.** Magnetic properties of  $\text{Mn}_6\text{O}(\text{VO}_4)_3(\text{OH})$ . (a) Temperature dependence of  $M/H$  measured in applied fields of  $H = 1$  and  $10$  kOe. (inset)  $H/M$  with a Curie–Weiss fit between  $100$  and  $300$  K. (b) Low-temperature behavior showing anomalies at  $3.7$  and  $26$  K. (c) Magnetic moment vs applied field measured at  $2$  and  $300$  K.

uncompensated components of the magnetic moments below  $T_N = 45$  K. **Figure 8b** shows the behavior of  $M/H$  below  $T_N$ . Two additional anomalies are observed at  $T_1 = 3.7$  K and  $T_2 = 26$  K. Since the anomaly at  $T_2$  is not seen in the lower-field data (**Figure 8a**), it may be associated with a transition that is induced by the applied field. The additional anomalies below  $T_N$  suggest that the spins may reorient upon further cooling below  $T_N$ , or that magnetic order develops in multiple stages, which may not be surprising considering there are five unique Mn sites, three with octahedral and two with trigonal bipyramidal coordination, and the main structural motif of the Mn sublattice is honeycomb-like.

Neutron diffraction studies would clearly be desirable to elucidate the complex magnetic behaviors suggested by the magnetization measurements of both  $\text{Mn}_5(\text{VO}_4)_2(\text{OH})_4$  and  $\text{Mn}_6\text{O}(\text{VO}_4)_3(\text{OH})$ , but the magnetization data strongly support a canted anti-ferromagnetic state in both materials at low temperature. As noted above, the magnetic sublattices in these compounds include honeycomb- and Kagome-like components. Both of these lattices support antisymmetric exchange interactions, also known as Dzyaloshinski–Moriya (DM) interactions.<sup>37–42</sup> Since these interactions favor perpendicular arrangements between neighboring spins, competition between DM and superexchange interactions may be the origin of the canted anti-ferromagnetic behavior seen in these compounds.

**3.5. Infrared and Raman Spectra of  $\text{Mn}_5(\text{VO}_4)_2(\text{OH})_4$  and  $\text{Mn}_6\text{O}(\text{VO}_4)_3(\text{OH})$ .** Infrared and Raman spectra are shown in Figure 9. This serves as qualitative confirmation of the OH

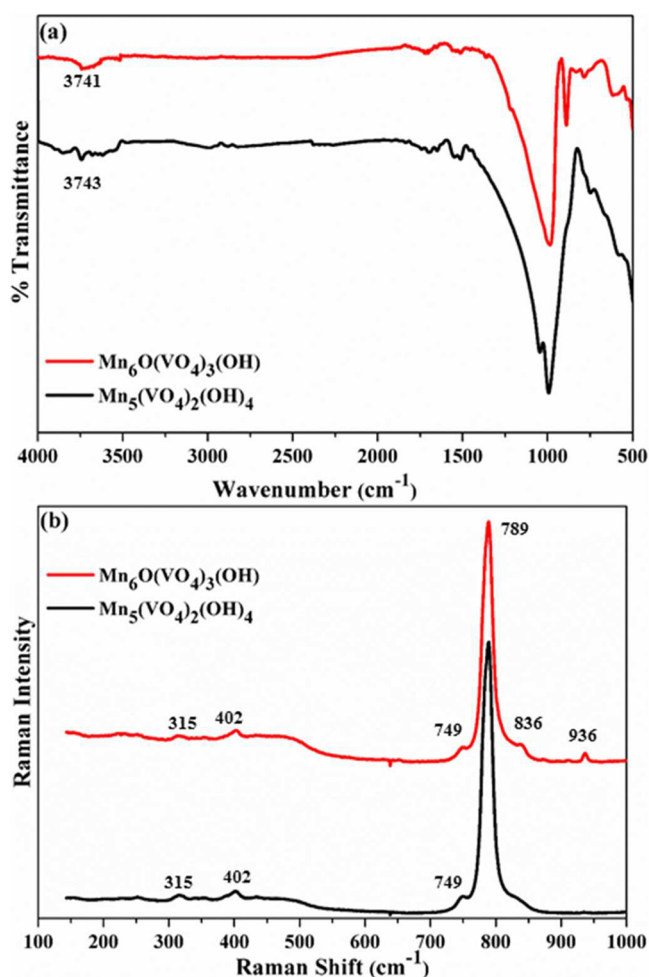


**Figure 9.** Infrared (a) and Raman (b) spectra for  $\text{Mn}_5(\text{VO}_4)_2(\text{OH})_4$  and  $\text{Mn}_6\text{O}(\text{VO}_4)_3(\text{OH})$ .

groups in the lattices. As expected, the stretching vibrations for O–H can be observed over the range of 3500–3750 cm<sup>-1</sup> for both  $\text{Mn}_5(\text{VO}_4)_2(\text{OH})_4$  and  $\text{Mn}_6\text{O}(\text{VO}_4)_3(\text{OH})$ , Figure 9a.<sup>43</sup> Additionally, bands at 1100–800 cm<sup>-1</sup> can be assigned to the tetrahedral  $[\text{VO}_4]$  groups. Raman bands (Figure 9b) above 700 cm<sup>-1</sup> are likely due to the stretching vibrations  $\nu_1$  of the  $[\text{VO}_4]$  groups. Both compounds exhibit a strong Raman band near 789 cm<sup>-1</sup>, likely the symmetric stretching mode of the vanadate

groups.<sup>2,6</sup> Weaker modes of  $[\text{VO}_4]$  groups are clearly visible in the Raman spectra near 740 and 840 cm<sup>-1</sup>, also within the expecting range for  $A_g$  and  $E_g$  modes.<sup>6,44,45</sup> It is noteworthy to mention that  $\text{Mn}_5(\text{VO}_4)_2(\text{OH})_4$  has only one unique  $[\text{VO}_4]$  group, while  $\text{Mn}_6\text{O}(\text{VO}_4)_3(\text{OH})$  has three crystallographically distinct  $[\text{VO}_4]$  groups. As a result, the additional bands at 838 and 936 cm<sup>-1</sup> in the Raman spectrum of  $\text{Mn}_6\text{O}(\text{VO}_4)_3(\text{OH})$  could be an indicator of the additional complexity of the  $[\text{VO}_4]$  groups in  $\text{Mn}_6\text{O}(\text{VO}_4)_3(\text{OH})$  compared to the  $\text{Mn}_5(\text{VO}_4)_2(\text{OH})_4$  Raman spectrum. The bands at 400 cm<sup>-1</sup> can be assigned to the  $[\text{VO}_4]$  antisymmetric bending modes. However, lattice mode vibrations (below 300 cm<sup>-1</sup>) are not clearly visible in both Raman spectra.

#### 4. SUMMARY AND CONCLUSION

Two new manganese vanadates have been synthesized as large single crystals using high-temperature hydrothermal growth methods. Both materials  $\text{Mn}_5(\text{VO}_4)_2(\text{OH})_4$  and  $\text{Mn}_6\text{O}(\text{VO}_4)_3(\text{OH})$  contain  $\text{Mn}^{2+}$  ions and have complex two-dimensional manganese oxide layers built of units consisting of  $\mu_3$ -oxo bridged manganese oxide trimers made of edge-shared  $\text{MnO}_6$  octahedra. The trimers form complex patterns of different planar honeycomb-like lattices. In  $\text{Mn}_6\text{O}(\text{VO}_4)_3(\text{OH})$ , the planar honeycomb substructures are connected through unusual  $[\text{Mn}_2\text{O}_8]$  dimers of trigonal bipyramidal building blocks to create an overall corrugated layer. In both structures, the vanadate groups serve as bridging groups linking the various building blocks together to overall form complex three-dimensional structures.

A previously reported compound,  $\text{K}_2\text{Mn}_3(\text{VO}_4)_2(\text{OH})_2$ , was also prepared using similar methods and serves as a prototype for manganese oxide layers built of  $[\text{Mn}_3\text{O}_{13}]$  trimeric building units, while also illuminating the descriptive chemistry encountered. In the case of this compound, the  $\text{K}^+$  ions from the mineralizer become incorporated in the structure and serve to separate the manganese-oxo layers creating a true two-dimensional layered structure. In the case of  $\text{Mn}_5(\text{VO}_4)_2(\text{OH})_4$  and  $\text{Mn}_6\text{O}(\text{VO}_4)_3(\text{OH})$ , various cesium salts were employed as mineralizers, and the  $\text{Cs}^+$  ion prefers to remain in solution and is not incorporated in the lattice. Thus, the vanadate groups cross-link the layers to form complex three-dimensional frameworks in those compounds. All three structure types exhibit different honeycomb-like structures of increasing complexity, and this suggests that a wide range of related complex manganese vanadates can be further prepared using this method.

The magnetic properties of  $\text{Mn}_5(\text{VO}_4)_2(\text{OH})_4$  and  $\text{Mn}_6\text{O}(\text{VO}_4)_3(\text{OH})$  were examined and indicated that both compounds have significant anti-ferromagnetic coupling with spin of 5/2 per Mn atom. Canted anti-ferromagnetic behavior is observed below Neel temperatures of 57 and 45 K, respectively. Additional magnetic ordering transitions occur at lower temperatures, as might be expected for such complex structures. More broadly, the materials reported here are the most recent in a rapidly growing family of transition-metal vanadates that contain intriguing structural and magnetic features, including the potentially magnetically frustrated honeycomb sublattices as building blocks. The high-temperature hydrothermal method not only leads to large high-quality single crystals of new compounds but the method also shows a significant sensitivity to reaction conditions, stoichiometries, and reagents. In particular, the vanadate group continues to display exceptionally varied and versatile behavior as a linking group and building

block. This rich chemistry suggests that we can continue to mine new materials with intriguing low-dimensional structures and interesting magnetic properties.

## ■ ASSOCIATED CONTENT

### Supporting Information

The Supporting Information is available free of charge on the ACS Publications website at DOI: 10.1021/acs.inorgchem.6b01286.

Crystal structure data in CIF format (CIF)

Table of elemental analyses, selected interatomic distances and angles for  $K_2M_3(VO_4)_2(OH)_2$  ( $M = Mn, Co$ ), optical micrograph of  $K_2Mn_3(VO_4)_2(OH)_2$  powder XRD patterns for composite reaction products (PDF)

## ■ AUTHOR INFORMATION

### Corresponding Author

\*E-mail: kjoseph@clemson.edu.

### Notes

The authors declare no competing financial interest.

## ■ ACKNOWLEDGMENTS

The authors thank the National Science Foundation Grant No. DMR-1410727 for financial support. Work at Oak Ridge National Laboratory was supported by the U.S. Department of Energy, Office of Science, Basic Energy Sciences, Materials Sciences and Engineering Division (magnetic studies).

## ■ REFERENCES

- (1) Schindler, M.; Hawthorne, F. C.; Baur, W. H. *Can. Mineral.* **2000**, *38*, 1443–1456.
- (2) Sun, K.; Litvinchuk, A. P.; Tapp, J.; Lorenz, B.; Möller, A. *Inorg. Chem.* **2015**, *54*, 898–904.
- (3) Zhang, F.; Zavalij, P. Y.; Whittingham, M. S. *J. Mater. Chem.* **1999**, *9*, 3137–3140.
- (4) Livage, J. *Coord. Chem. Rev.* **1998**, *178–180*, 999–1018.
- (5) Chirayil, T.; Zavalij, P. Y.; Whittingham, M. S. *Chem. Mater.* **1998**, *10*, 2629–2640.
- (6) Bratsch, M.; Tapp, J.; Litvinchuk, A. P.; Möller, A. *Inorg. Chem.* **2014**, *53*, 4994–5001.
- (7) Nakayama, G.; Hara, S.; Sato, H.; Narumi, Y.; Nojiri, H. *J. Phys.: Condens. Matter* **2013**, *25*, 116003.
- (8) Clemens, O.; Rohrer, J.; Nenert, G. *Dalton Trans.* **2016**, *45*, 156–171.
- (9) Wang, X.; Liu, Z.; Ambrosini, A.; Maignan, A.; Stern, C. L.; Poeppelmeier, K. R.; Dravid, V. P. *Solid State Sci.* **1998**, *2*, 99–107.
- (10) Möller, A.; Amunke, N. E.; Daniel, P.; Lorenz, B.; de la Cruz, C. R.; Gooch, M.; Chu, P. C. W. *Phys. Rev. B: Condens. Matter Mater. Phys.* **2012**, *85*, 214422.
- (11) Amunke, N. E.; Tapp, J.; De la Cruz, C.; Möller, A. *Chem. Mater.* **2014**, *26*, 5930–5935.
- (12) Freedman, D. E.; Chisnell, R.; McQueen, T. M.; Lee, Y. S.; Payen, C.; Nocera, D. G. *Chem. Commun.* **2012**, *48*, 64–68.
- (13) Lawes, G.; Harris, A. B.; Kimura, T.; Rogado, N.; Cava, R. J.; Aharony, A.; Entin-Wohlman, O.; Yildirim, T.; Kenzelmann, M.; Broholm, C.; Ramirez, A. P. *Phys. Rev. Lett.* **2005**, *95*, 087205.
- (14) Dai, D.; Whangbo, M. H. *J. Chem. Phys.* **2004**, *121*, 672.
- (15) Whangbo, M. H.; Dai, D.; Koo, H. *Solid State Sci.* **2005**, *7*, 827.
- (16) Geertsma, W.; Khomskii, D. *Phys. Rev. B: Condens. Matter Mater. Phys.* **1996**, *54*, 3011–3014.
- (17) Fields, R. A.; Birnbaum, M.; Fincher, C. L. *Appl. Phys. Lett.* **1987**, *51*, 1885–1886.
- (18) Forbes, A. R.; McMillen, C. D.; Giesber, H. G.; Kolis, J. W. *J. Cryst. Growth* **2008**, *310*, 4472–4476.
- (19) Kolis, J. W.; Syracuse, S. J. USPTO 7,211,234 May 1, 2007.
- (20) Kimani, M. M.; Thompson, L.; Snider, W.; McMillen, C. D.; Kolis, J. W. *Inorg. Chem.* **2012**, *51*, 13271–13280.
- (21) Kimani, M. M.; McMillen, C. D.; Kolis, J. W. *Inorg. Chem.* **2012**, *51*, 3588–3596.
- (22) Kimani, M. M.; Kolis, J. W. *J. Lumin.* **2014**, *145*, 492–497.
- (23) Sanjeeva, L. D.; McGuire, M. A.; Garlea, V. O.; Hu, L.; Chumanov, G.; McMillen, C. D.; Kolis, J. W. *Inorg. Chem.* **2015**, *54*, 7014–7020.
- (24) Sanjeeva, L. D.; Garlea, V. O.; McGuire, M. A.; McMillen, C. D.; Cao, H. B.; Kolis, J. W. *Phys. Rev. B: Condens. Matter Mater. Phys.* **2016**, DOI: 10.1103/PhysRevB.93.224407.
- (25) *CrystalClear*; Rigaku and Molecular Structure Corporation: The Woodlands, TX, 2006.
- (26) Sheldrick, G. M. *Acta Crystallogr., Sect. A: Found. Crystallogr.* **2008**, *64*, 112–122.
- (27) Brese, N. E.; O’Keeffe, M. *Acta Crystallogr., Sect. B: Struct. Sci.* **1991**, *47*, 192–197.
- (28) Brown, I. D.; Altermatt, D. *Acta Crystallogr., Sect. B: Struct. Sci.* **1985**, *41*, 244–247.
- (29) Basso, R.; Luchetti, G.; Zefiro, L. *Rigaku Journal* **2010**, *26*, 23–27.
- (30) Basso, R.; Lucchetti, G.; Zefiro, L.; Palenzona, A. Z. *Kristallogr.* **1992**, *201*, 223–234.
- (31) Liao, H.; Guyomard, D.; Piffard, Y.; Tournoux, M. *Acta Crystallogr., Sect. C: Cryst. Struct. Commun.* **1996**, *52*, 284–286.
- (32) Wang, X.-D.; Liu, Z.-Q.; Ambrosini, A.; Maignan, A.; Stern, C. L.; Poeppelmeier, K. R.; Dravid, V. P. *Solid State Sci.* **1998**, *2*, 99–107.
- (33) Shimokawa, T.; Nakano, H. *J. Phys. Soc. Jpn.* **2012**, *81*, 084710.
- (34) Sun, K.; Moeller, A. *Acta Crystallogr., Sect. E: Struct. Rep. Online* **2014**, *70*, i33.
- (35) Shannon, R. D. *Acta Crystallogr., Sect. A: Cryst. Phys., Diffraction, Theor. Gen. Crystallogr.* **1976**, *32*, 751–767.
- (36) Yakubovich, O. V.; Yakovleva, E. V.; Golovanov, A. N.; Volkov, A. S.; Volkova, O. S.; Zvereva, E. Z.; Dimitrova, O. V.; Vasiliev, A. N. *Inorg. Chem.* **2013**, *52*, 1538–1543.
- (37) Dzyaloshinsky, I. *J. Phys. Chem. Solids* **1958**, *4*, 241–255.
- (38) Moriya, T. *Phys. Rev.* **1960**, *120*, 91–99.
- (39) Okubo, S.; Ueda, T.; Ohta, H.; Zhang, W.; Sakurai, T.; Onishi, N.; Azuma, M.; Shimakawa, Y.; Nakano, H.; Sakai, T. *Phys. Rev. B: Condens. Matter Mater. Phys.* **2012**, *86*, 140401.
- (40) Fujita, T.; Yamaguchi, H.; Kimura, S.; Kashiwagi, T.; Hagiwara, M.; Matan, K.; Grohol, D.; Nocera, D. G.; Lee, Y. S. *Phys. Rev. B: Condens. Matter Mater. Phys.* **2012**, *85*, 094409.
- (41) Elhajal, M.; Canals, B.; Lacroix, C. *Phys. Rev. B: Condens. Matter Mater. Phys.* **2002**, *66*, 014422.
- (42) Okuta, K.; Hara, S.; Sato, H.; Narumi, Y.; Kindo, K. *J. Phys. Soc. Jpn.* **2011**, *80*, 063703.
- (43) Frost, R. L.; Erickson, K. L.; Weier, M. L. *Spectrochim. Acta, Part A* **2004**, *60*, 2419–2423.
- (44) Frost, R. L.; Palmer, S. J.; Cejka, J.; Sejkora, J.; Plasil, J.; Bahfenne, S.; Keeffe, E. C. *J. Raman Spectrosc.* **2011**, *42*, 1701–1710.
- (45) Frost, R. L.; Erickson, K. L.; Weier, M. L.; Carmody, O. *Spectrochim. Acta, Part A* **2005**, *61*, 829–834.